Intertwining of multiphase charge density waves in In-intercalated $TaSe_2$

Ningning Liu,[1] Yupeng Li,[2,3] Ping Li,[4] Gang Yao,[1] Yueqiao Qu,[1] Yanfu Wu,[1] Dan-Dan Guan,[1,5] Shiyong Wang,[1,5] Hao Zheng,[1,5] Yao-Yi Li,[1,5] Zhu-An Xu,[2,5] Weidong Luo,[1,5] Canhua Liu,[1,5,6,*] and Jin-Feng Jia[1,5,6]

[1]*Key Laboratory of Artificial Structures and Quantum Control (Ministry of Education), Shenyang National Laboratory for Materials Science, School of Physics and Astronomy, Shanghai Jiao Tong University, 800 Dongchuan Road, Shanghai 200240, China*

[2]*Zhejiang Province Key Laboratory of Quantum Technology and Device, Department of Physics, Zhejiang University, Hangzhou 310027, China*

[3]*Beijing National Laboratory for Condensed Matter Physics, Institute of Physics, Chinese Academy of Sciences, Beijing 100190, China*

[4]*Key Laboratory of Advanced Electronic Materials and Devices, School of Mathematics and Physics, Anhui Jianzhu University, Hefei 230601, China*

[5]*Collaborative Innovation Center of Advanced Microstructures, Nanjing 210093, China*

[6]*Tsung-Dao Lee Institute, Shanghai 200240, China*

(Received 10 August 2021; revised 1 November 2021; accepted 3 November 2021; published 9 December 2021)

Disorder caused by defects plays an important role on the emergence of exotic physical phenomena in quantum states of materials, including charge density waves (CDWs). Usually, the coexistence of multiphase CDWs aroused by defects is manifested in multiple domains resulting from phase separation. By using scanning tunneling microscopy, we reveal an intertwining of two CDW phases without explicit domain boundaries on a cleaved surface of layered intercalation compounds In_xTaSe_2 ($x = 0.58$), which undergoes commensurate CDW transitions twice by cooling. The two CDW phases, i.e., $2 \times \sqrt{3}$ and 2×2 phases at higher and lower temperature, respectively, have very similar atomic arrangements in the $TaSe_2$ layers and thus are very sensitive to the random potentials induced by the intercalated In atoms. Moreover, the translational symmetry breaking of the $2 \times \sqrt{3}$ phase results in the presence of another intertwined $\sqrt{7} \times \sqrt{7}$ phase. These findings provide insight into the microscopic effect of defects on multiphase CDWs and reveal a coexisting manner of CDW phases.

DOI: 10.1103/PhysRevB.104.235410

I. INTRODUCTION

Charge density waves (CDWs) are spatially modulated electronic charge density accompanied by a periodic lattice distortion [1–8]. Both the static and dynamic properties of the CDW states are substantially influenced by the interaction between the CDWs and the inevitably existing impurities that provide a random potential field coupling linearly to the order parameter [9]. The CDW phase will be pinned at each impurity site if the impurity potential is strong enough, or it will be pinned collectively so that CDW phase domains come into form in the weak pinning region [10–16]. Owing to the development of scanning tunneling microscopy (STM), the pinning effects of the impurities to the CDW states have been directly imaged in quasi-low-dimensional materials, including transition-metal dichalcogenides (TMDs) and metal-absorbed surface superstructures [17–20]. For example, the CDWs in $Nb_xTa_{1-x}S_2$ exhibit a two-dimensional meltinglike phase transition as the impurity concentration increases [21]. The CDWs in $NbSe_2$, being subject to locally strong pinning, show a Bragg glass phase accompanied by bound dislocation-antidislocation pairs near the impurities [12]. Intrinsic solitons trapped by impurities are clearly distinguished as characteristic variations of the CDW amplitude in In atomic wire arrays on Si(111) [22,23]. In most cases these studies have focused on the effects of impurities to the CDW phase in a single domain. While some TMDs undergo CDW transitions twice as temperature decreases [24–26], it would be interesting to unveil the effects of impurities to the two CDW phases that may coexist in a certain temperature window.

$2H$-$TaSe_2$ is a typical TMD having a layered structure in which each layer consists of a Se-Ta-Se sandwich with strong ionic bonds within a local trigonal prismatic unit. It undergoes an incommensurate CDW transition at ∼122 K, followed by a lock-in transition towards a commensurate 3×3 CDW phase at ∼90 K, and finally to a superconducting state at ∼0.14 K [26–28]. Intercalation of metal atoms between the $TaSe_2$ layers leads to interesting phenomena. For instance, the Ni or Pd intercalation raises the superconducting transition temperature [29,30], while the Pb, Tl, or In intercalation induces topological band structures [31–33]. Meanwhile, the intercalated metal atoms may introduce random potentials to the TMD layers, which makes it a good platform for studying the interplay between disorders and CDWs with multiphases.

Here we present an STM study on an In-intercalated $TaSe_2$ crystal ($In_{0.58}TaSe_2$) that undergoes CDW transitions twice with critical temperatures of $T_1 = 116$ K and $T_2 = 77$ K revealed in previous transport measurements [33]. The STM images taken at various temperatures show that both intrinsic CDWs are commensurate, i.e., $2 \times \sqrt{3}$ and 2×2 phases at

*Author to whom correspondence should be addressed: canhualiu@sjtu.edu.cn

higher and lower temperature, respectively. Due to the random potentials produced by the intercalated In atoms, another commensurate $\sqrt{7} \times \sqrt{7}$ phase is observed to be intertwined with the $2 \times \sqrt{3}$ phase below T_1. Moreover, the $2 \times \sqrt{3}$ and 2×2 phases are also intertwined at temperatures between T_1 and T_2. The intertwining of the two CDW phases makes them difficult to be distinguished directly in STM images without performing Fourier transform of the images. This is quite different from previous STM images of TMDs, where CDWs usually present in distinct domains with single phases and can be well distinguished in the appearance of phase separation.

II. METHODS

The $In_{0.58}TaSe_2$ single crystal was synthesized by vapor transport methods in which polycrystalline $InTaSe_2$ was sealed in an evacuated ampoule with a length of 16 cm and iodine/$InBr_3$ was used as transport agent (5 mg/cm^3). Several platelike In_xTaSe_2 single crystals with similar $x \sim 0.6$ were grown in a two-zone furnace by setting the powder end at 1123 K and the cooler end at 1023 K for three weeks. The structure and composition ratio of the sample used in the present work were confirmed by x-ray diffraction (XRD) and energy-dispersive x-ray spectroscopy, respectively [33]. The $In_{0.58}TaSe_2$ single crystal was cleaved at room temperature after being thoroughly outgassed at ~160 °C in a UHV STM system (Unisoku USM1400) and then transferred to a sample stage attached to a cryogenic tank for STM observations at varied temperatures. The sample temperature higher than 77 K was controlled by heating the sample stage with a feedback controller (Cryogenic Control systems, model 32B temperature controller). The STM data of 7.8 K were taken in another UHV-STM system (Unisoku USM1300 STM+ model) [34,35].

Density functional theory (DFT) calculations were performed using the generalized-gradient approximation (GGA) under the Perdew-Burke-Ernzerhof (PBE) parameterization, as implemented in the Vienna Ab Initio Simulation Package (VASP) [36]. The wave functions are expanded in plane-wave basis with a kinetic energy cutoff of 400 eV. The crystal structures are optimized until the residual forces on each atom are smaller than 0.02 eV/Å. The Γ-centered $8 \times 8 \times 6$ and $7 \times 8 \times 6$ Monkhorst-Pack k-point meshes were employed for the $2 \times 2 \times 1$ and $2 \times \sqrt{3} \times 1$ supercells, respectively.

III. RESULTS AND DISCUSSION

The compound $InTaSe_2$ has a noncentrosymmetric structure with two adjacent $TaSe_2$ layers intercalated by an In layer, as schematically illustrated in Fig. 1(a). It belongs to the hexagonal crystal system, formed in the space group $P\bar{6}m2$ (No. 187), and has the same structure as $TlTaSe_2$ [32]. For the $In_{0.58}TaSe_2$ sample used in the present work, the intercalated In atoms distribute randomly and uniformly in the interlayers. After cleavage, the exposed In atoms tend to aggregate and form amorphous In clusters in some surface areas, thus leaving other large clean surface areas without In adatoms. It is not surprising to find no individual intercalated adatoms on the surface, since previous STM observations performed on Fe-intercalated 2H-$TaSe_2$ found no Fe adatoms on the Se-terminated surface [37]. Figure 1(b) is a typical STM image taken on the clean surface region at 127 K, showing a 1×1 lattice with a unit-cell size of $a = 3.46$ Å determined by XRD [33]. Each bright protrusion corresponds to the location of a Se atom in the upmost layer. The fast Fourier transform (FFT) of the STM image gives a set of 1×1 Bragg spots, as shown in the inset of Fig. 1(b). It is in sharp contrast to those taken at lower temperatures, displaying abundant Bragg spots arising from additional periodicities including $2 \times \sqrt{3}$, $\sqrt{7} \times \sqrt{7}$, and 2×2, as revealed below. These periodic lattices with respect to the upmost Se atomic sites in real space are schematically illustrated in Fig. 1(c), and the Bragg spots aroused by these lattices in reciprocal space are shown in Fig. 1(d) for reference.

When the $In_{0.58}TaSe_2$ sample is cooled to 112 K, slightly lower than T_1, the STM image with atomic resolution shows a faint but discernable modulation arising from the formation of CDW. The modulation superimposed on the 1×1 lattice shows $\times\sqrt{3}$ and $\times 2$ periodicities along the mutually perpendicular directions of $[1\bar{1}0]$ and [110], respectively, as denoted by arrows in Fig. 2(a). The $2 \times \sqrt{3}$ periodicity manifests itself explicitly in FFT of the STM image, where an additional set of Bragg spots indicative of a $\sqrt{7} \times \sqrt{7}$ periodicity also exist, as shown in Fig. 2(b). It is noted that the $2 \times \sqrt{3}$ spots have a higher intensity than the $\sqrt{7} \times \sqrt{7}$ spots and thus are not the high-order reflections from the latter. Interestingly, one cannot distinguish any domain with a single phase of $2 \times \sqrt{3}$ or $\sqrt{7} \times \sqrt{7}$ in the STM image, which is in sharp contrast to those of other TMD compounds showing distinct phase separation in real space [6,13,16,38]. The lack of a distinct domain boundary can be further demonstrated by dividing the STM image into nine subregions, each of which exhibits both the $2 \times \sqrt{3}$ and $\sqrt{7} \times \sqrt{7}$ phases in its FFT pattern, and the Bragg-spot intensity of the two intertwined phases shows an apparent spatial inhomogeneity, as show in Fig. S1 [39].

The two phases of $2 \times \sqrt{3}$ and $\sqrt{7} \times \sqrt{7}$ intertwine with each other because they have a strong relationship in atomic arrangement. As seen in Fig. 1(c), the $\sqrt{7} \times \sqrt{7}$ lattice may be transformed from the $2 \times \sqrt{3}$ lattice by breaking translational symmetry of the latter's corner atoms in both directions of $[1\bar{1}0]$ and [110] while keeping the opposing corner atoms identical. The main difference between the two lattices in the atomic arrangement is that the periodicity along the Se atomic rows containing corner atoms in [110] direction, i.e., L_A (or L_C) denoted in Fig. 1(c), is $\times 2$ in the $2 \times \sqrt{3}$ lattice while $\times 4$ in the $\sqrt{7} \times \sqrt{7}$ lattice. When the intertwining of the two phases occurs, one may find both $\times 2$ and $\times 4$ modulations along L_A lines. This is exactly what we have found in the STM observations. The line profiles of two adjacent lines arbitrarily drawn in Fig. 2(a) are displayed in the upper two panels of Fig. 2(d), where L_{A1} corresponding to L_A shows a modulation with intertwined $\times 2$ and $\times 4$ periodicities superimposed on a $\times 1$ modulation, while L_{B1} corresponding to the adjacent Se atomic row, i.e., L_B denoted in Fig. 1(c), shows mainly the $\times 1$ modulation.

Based on the relationship in atomic arrangement, it is reasonable to believe that the emergence of the $2 \times \sqrt{3}$ lattice is due to the formation of CDW in the $TaSe_2$ layer, while the intertwined $\sqrt{7} \times \sqrt{7}$ periodicity results from the intercalation of In atoms that generate a random potential, inducing a

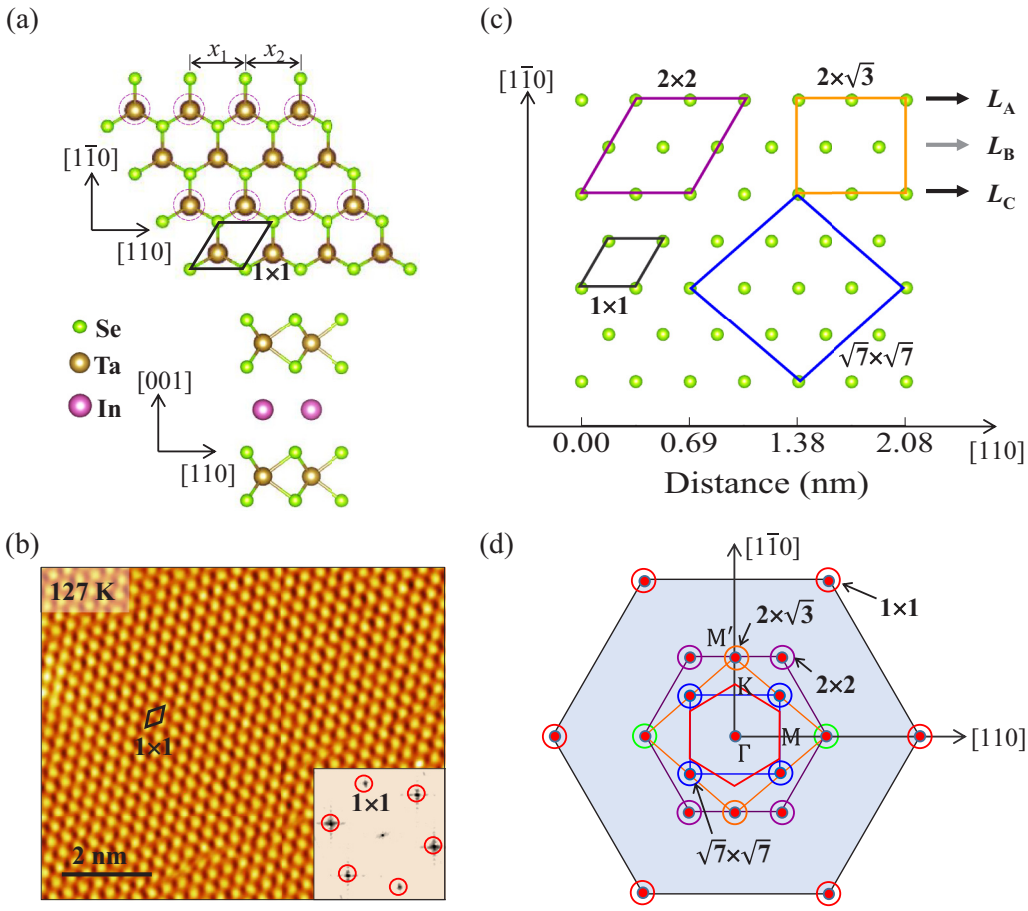

FIG. 1. (a) Top (upper) and side (lower) views of atomic structure of the compound $InTaSe_2$. The broken circles indicate the occupation of In atoms in a 2×2 model of $In_{0.5}TaSe_2$. x_1 and x_2 are the separations of neighbor Ta atoms along the [110] direction. (b) STM topography of the cleaved $In_{0.58}TaSe_2$ single crystal taken at 127 K, $V_s = -190$ mV and $I = 100$ pA. Insert: FFT pattern. (c) Schematic plots of the unit cells of $\sqrt{7} \times \sqrt{7}$, $2 \times \sqrt{3}$, 2×2, and 1×1 superimposed on the topmost Se atomic sites. (d) Schematic diagram of the unit cells in reciprocal space. The Bragg spots circled in varied colors are from different unit cells as indicated in the figure. The color notation here is applicable to all FFT patterns. The red hexagon represents the Brillouin zone of a 2×2 superlattice.

strong phase fluctuation and thus destroying the long-range order of the $2 \times \sqrt{3}$ CDW phase. The main feature of the quasi-ordered CDW phase observed in the STM images can be reproduced by introducing a phase fluctuation caused by the intercalated In atoms. The local density of states (LDOS) in the surface, $\rho(\boldsymbol{r})$, is a linear superposition of two parts [12,40,41]: one is from the 1×1 host lattice, $\rho_{\rm av}(\boldsymbol{r})$, and the other from the CDW modulation, $\delta\rho(\boldsymbol{r})$. The latter determines the additional periodic feature of the STM images and is written as

$$\delta\rho(\boldsymbol{r}) = \sum_i \mathrm{Re}[\psi_i(\boldsymbol{r}) e^{j\pi \boldsymbol{Q}_i \cdot \boldsymbol{r}}]. \tag{1}$$

Here $\boldsymbol{Q}_i$ is the CDW wave vector corresponding to the ith Bragg spot, and ψ_i is the order parameter given by

$$\psi_i(r) = \rho_i e^{j[\phi_i - \tilde{\phi}_i(r)]}, \tag{2}$$

where ρ_i is the amplitude proportional to the intensity of each Bragg spot, ϕ_i is the phase without perturbation, and $\tilde{\phi}_i$ is the phase deviation describing the phase fluctuation. In practice, the spatial variation of $\tilde{\phi}_i$ is given by a random number extracted from the normal distribution $N(\mu_i, \sigma^2)$, with the mean $\mu_i = \phi_i$ and the standard deviation σ set to be 0.4π for simplicity.

The intensity ratio between the Bragg spots of the $2 \times \sqrt{3}$ and $\sqrt{7} \times \sqrt{7}$ phases is about 1.6 ± 0.4, as revealed in Fig. 2(b), so the LDOS map is calculated from the above two equations by using the intensity ratio of 1.5 and is displayed in Fig. 2(c). Very similar to the STM image, the calculated LDOS map shows the $\times\sqrt{3}$ and $\times 2$ modulations along [1$\bar{1}$0] and [110] directions, respectively, while its FFT shows both $2 \times \sqrt{3}$ and $\sqrt{7} \times \sqrt{7}$ periodicities. Two adjacent rows, L_{A2} and L_{B2}, along [110] direction, are arbitrarily chosen in Fig. 2(c) for plotting the line profiles displayed in the lower two panels of Fig. 2(d). Only on L_{A2} can one see the intertwined $\times 2$ and $\times 4$ periodicities superimposed on the $\times 1$ modulation, which reproduces well the feature on L_{A1} taken from the STM image. These similarities between the STM image and the calculated LDOS map strongly imply that the introduction of CDW phase fluctuation should be reasonable for the interpretation of the intertwining of the $\sqrt{7} \times \sqrt{7}$ and $2 \times \sqrt{3}$ periodicities.

As temperature decreases, previous work has revealed a second but more gradual CDW phase transition at around

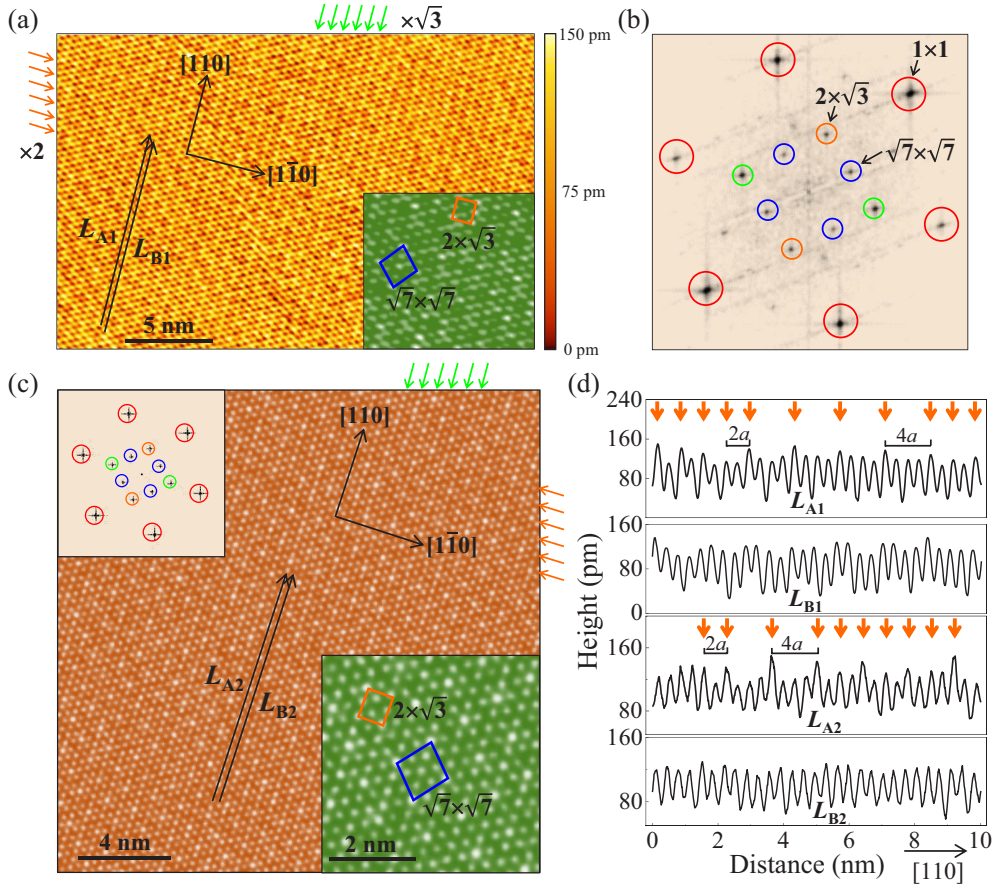

FIG. 2. (a) STM topography taken at 112 K, $V_s = -350$ mV and $I = 100$ pA. Arrows above and beside the image indicate the modulations of the $2 \times \sqrt{3}$ CDWs. Insert: zoom-in STM image taken in the same condition. (b) FFT pattern of the STM image in (a). (c) Calculated LDOS map taking phase fluctuations into account. Upper-left insert: FFT pattern of the map. Bottom-right insert: zoom-in map. (d) Line profiles along the lines drawn in (a) and (c). Arrows denote the higher peaks showing double or quadruple periodicities on L_{A1} and L_{A2}.

77 K in electronic transport measurements, and the lower-temperature CDW phase exhibits a 2×2 periodicity in STM observations [33]. Figure 3(a) shows a typical STM image taken at 82 K in which one seems to recognize the 2×2 unit cell as the rhombus denotes. However, the FFT of the STM image exhibits another two sets of Bragg spots corresponding to $\sqrt{7} \times \sqrt{7}$ and $2 \times \sqrt{3}$ besides the 2×2 periodicity, as shown in Fig. 3(b). As a consequence of higher-order harmonics, several additional spots not circled in the figure are also seen. It is noted that the coexistence of three sets of Bragg spots in the FFT pattern is not due to phase separation. The FFT pattern of any 1/8 part of the STM image exhibits at least two sets of the Bragg spots resulting from the $2 \times \sqrt{3}$ and 2×2 periodicities, and the Bragg-spot intensity of each of the phases has apparent spatial inhomogeneity, as shown in Fig. S2 [39]. As an example, the inset of Fig. 3(a) shows the FFT of the upper-left corner of the image, where the $\sqrt{7} \times \sqrt{7}$ spots are not visible.

Another fact shows no phase separation is seen in the zoom-in STM image displayed in Fig. 3(d), where three quadrangles are superimposed to denote the three kinds of periodicities. Comparing with Fig. 1(c), it is easy to find that each protrusion in the STM image still corresponds to the upmost Se atomic site. The protrusions with varied brightness on the Se rows denoted by L_A and L_C [following the notations in Fig. 1(c)] are separated equally, while those on the Se rows of L_B appear as dimmers. This is more explicitly demonstrated in the line profiles shown in Fig. 3(c), which are arbitrarily taken along three adjacent Se atomic rows in the STM image of Fig. 3(a). The three phases, i.e., $\sqrt{7} \times \sqrt{7}$, $2 \times \sqrt{3}$, and 2×2, may have very similar atomic structures and differ mainly in the atomic arrangement along the rows of L_A and L_C. In contrast to the $\sqrt{7} \times \sqrt{7}$ phase having a $\times 4$ modulation, both of the other two phases have a $\times 2$ modulation along the rows of L_A and L_C. The $\times 2$ modulations on the two rows are in-phase for the $2 \times \sqrt{3}$ phase but opposite in phase for the 2×2 phase, as discovered by comparing the positions of the brighter protrusions [denoted by arrows in Fig. 3(c)] along the rows of L_{A3} with those along L_{C3}. Such a peculiar difference in the atomic arrangement between the $2 \times \sqrt{3}$ and 2×2 phases results in the intertwining of the two phases, and the lack of long-range order is associated with strong phase fluctuations caused by the randomly dispersed In atoms in the intercalation layers.

As temperature further decreases, the whole surface exhibits the 2×2 phase, as observed in the STM image and its FFT pattern shown in Fig. 4. This means the 2×2 phase should be energetically more stable than the $2 \times \sqrt{3}$ phase. It is a reasonable result when considering that the 2×2 lattice has the same lateral symmetry as that of the host 1×1 lattice

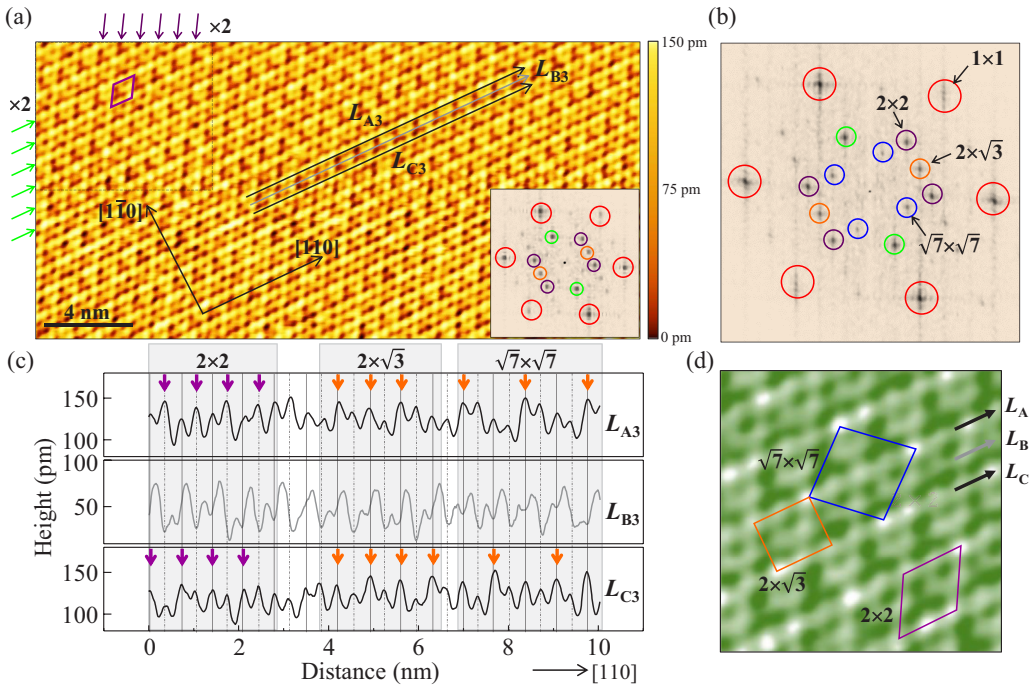

FIG. 3. (a) STM topography taken at 82 K, $V_s = 1$ V and $I = 100$ pA. Arrows above and beside the image indicate the modulations of the 2×2 CDWs. Insert: FFT pattern of the upper-left corner enclosed by the dashed quadrangle. (b) FFT pattern of the whole STM image in (a). (c) Line profiles along the lines drawn in (a). Arrows denote the higher peaks showing double or quadruple periodicities on L_{A3} and L_{C3}. The alternating solid and dashed lines are separated by a. (d) Zoom-in STM image taken in the same conditions as (a). Three arrows indicate three Se atomic rows as those shown in Fig. 1(c).

while the $2 \times \sqrt{3}$ does not. Since the $\sqrt{7} \times \sqrt{7}$ phase results from the translational symmetry breaking of the $2 \times \sqrt{3}$ phase as discussed above, it also fades out with the $2 \times \sqrt{3}$ phase during the sample cooling.

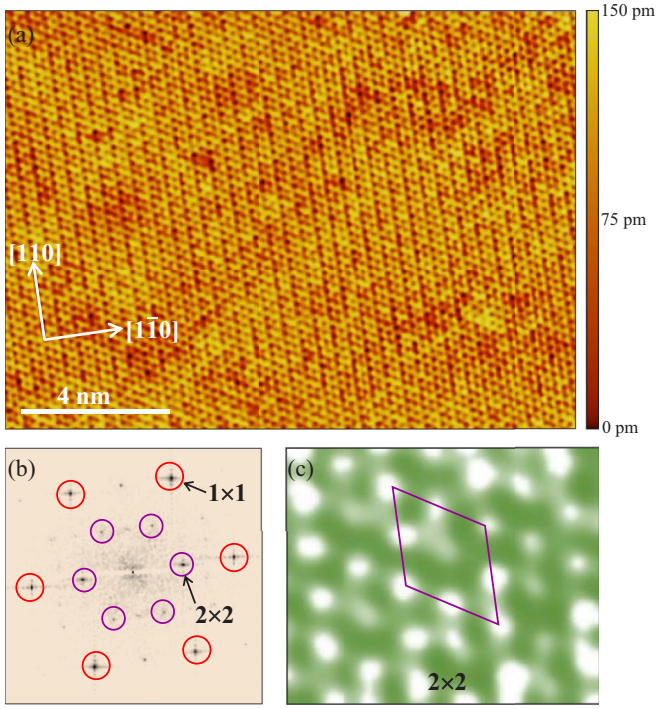

FIG. 4. (a) STM topography taken at 7.8 K, $V_s = 600$ mV, and $I = 100$ pA. (b) FFT pattern of (a). (c) Zoom-in STM image taken in the same conditions as (a).

The stoichiometric ratio of $In_{0.58}TaSe_2$ investigated here is very close to that of $In_{0.5}TaSe_2$, so roughly there are two intercalated In atoms in each $2 \times \sqrt{3}$ or 2×2 unit cell on average. Each In atom locates beneath one Ta site, as illustrated in Fig. 1(a), and the four possible sites for the occupation of two In atoms in each unit cell are equivalent. Therefore, first-principles calculations were performed with the atomic structures of $In_{0.5}TaSe_2$, in which In atoms form an array of atomic chains along the [110] direction, as the broken circles indicate in Fig. 1(a). Figure 5(a) shows the calculated formation energy ΔE as a function of the relative displacement of Ta atoms $\delta\text{Ta} = |x_2 - x_1|/2$ along [110], since the displacement of Ta atoms along the [1$\bar{1}$0] direction is negligible. Here, ΔE is defined as the relative total energy of each supercell with respect to that with $\delta\text{Ta} = 0$ Å. The formation energy of the 2×2 structure is always smaller than that of the $2 \times \sqrt{3}$ structure, which is consistent with the STM observations at 7.8 K. More importantly, both the $2 \times \sqrt{3}$ and 2×2 supercells show energy minima at the same and tiny displacement $\delta\text{Ta} = 0.01$ Å, where the energy difference is very small (~2 meV). These make it possible for the two phases intertwining with each other at an elevated temperature, especially when the location of In atoms lacks long-range order.

Besides the 2×2 supercell model studied above (low-T model), we also calculated another 2×2 supercell model in which the Se atoms are fixed in a 1×1 surface lattice to represent the 1×1 phase observed at high temperature (high-T model). Naturally, the lowest formation energy of the low-T

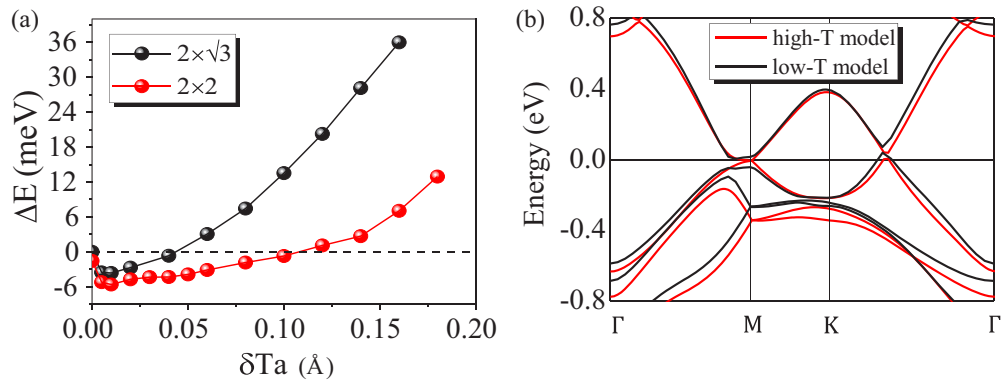

FIG. 5. The first-principles calculation of $In_{0.5}TaSe_2$. (a) Calculated formation energy ΔE as a function of relative displacement of Ta atoms, $\delta\text{Ta} = |x_2 - x_1|/2$ in a $2 \times \sqrt{3}$ or 2×2 supercell. (b) Band structures calculated with 2×2 supercells of the high-T and low-T models.

model is about 45 meV lower than that of the high-T model. The calculated band structures of the two atomic models show similar dispersion, as shown in Fig. 5(b). The main difference is that an energy gap opens at the Fermi level at M point in the low-T model, which may contribute to the CDW formation. In a previous work of angle-resolved photoemission spectroscopy (ARPES) on $In_{0.58}TaSe_2$, however, an energy gap was observed at the M' point [marked in Fig. 1(d)] but not M point [33], although the two points are equivalent in a 2×2 Brillouin zone. The band structure of $InTaSe_2$ with a 1×1 supercell was calculated for the interpretation of the ARPES results, despite that the measurements were performed on a 2×2 phase of $In_{0.58}TaSe_2$ at low temperature [33]. The discrepancy between the ARPES results and the DFT calculations comes from the fact that the intercalated In atoms are not aligned in a long-range order, whose effect on the band structure is difficult to be accurately reproduced. The opened gap at the M point found in calculations may be smeared out by the disordered In distribution, which requires more efforts to unveil the mechanism of the CDW transition.

IV. CONCLUSION

As a summary, our STM observations reveal intertwining of two CDW phases with $2 \times \sqrt{3}$ and 2×2 periodicities in an In-intercalated $TaSe_2$ crystal surface, where the In atoms generate a randomly distributed potential to the adjacent $TaSe_2$ layers that undergo commensurate CDW transitions twice as temperature decreases. The two CDWs coexisting in a certain temperature window cannot be distinguished directly in real space since their translational order is disturbed by the presence of random potential. However, they are manifested in reciprocal space by exhibiting sharp Bragg spots in the FFT pattern of the STM images, which means their orientational order is well maintained. Moreover, the translational symmetry breaking of the $2 \times \sqrt{3}$ CDW phase due to the random potentials results in the presence of an intertwined $\sqrt{7} \times \sqrt{7}$ phase. Such an intertwining of multiple phases hinders the formation of domains, resulting in a new coexisting manner of CDW phases. It is noted that most intercalated TMDs, including $PbTaSe_2$, $TlTaSe_2$, and $InTaSe_2$, have topologically nontrivial bands [31–33], which may have interplay with CDWs introduced by the imperfect intercalation of metal atoms in compound M_xTaSe_2 and thus generate fascinating phenomena, such as three-dimensional quantum Hall effects [42,43] and axionic quasiparticles [44,45]. In this sense the intertwining of CDWs revealed in compound $In_{0.58}TaSe_2$ could be generalized to other imperfectly intercalated TMD compounds and is worthy of further study with regard to its interplay with topological states.

ACKNOWLEDGMENTS

We thank the Ministry of Science and Technology of China (Grants No. 2019YFA0308600 and No. 2020YFA0309000), the NSFC (Grants No. 11874256, No. 11521404, No. 11634009, No. 92065201, No. 11874258, No. 12074247, No. 11790313, No. 11774305, and No. 11861161003), the Strategic Priority Research Program of the Chinese Academy of Sciences (Grant No. XDB28000000), and the Science and Technology Commission of Shanghai Municipality (Grants No. 2019SHZDZX01, No. 19JC1412701, and No. 20QA1405100) for partial support.

[1] S. H. Liu, Charge-density-wave state in VS, Phys. Rev. B **10**, 3619 (1974).

[2] E. Morosan, H. W. Zandbergen, B. S. Dennis, J. W. G. Bos, Y. Onose, T. Klimczuk, A. P. Ramirez, N. P. Ong, and R. J. Cava, Superconductivity in Cu_xTiSe_2, Nat. Phys. **2**, 544 (2006).

[3] T. Kiss, T. Yokoya, A. Chainani, S. Shin, T. Hanaguri, M. Nohara, and H. Takagi, Charge-order-maximized momentum-dependent superconductivity, Nat. Phys. **3**, 720 (2007).

[4] H. Cercellier, C. Monney, F. Clerc, C. Battaglia, L. Despont, M. G. Garnier, H. Beck, P. Aebi, L. Patthey, H. Berger, and L. Forró, Evidence for an Excitonic Insulator Phase in 1T-$TiSe_2$, Phys. Rev. Lett. **99**, 146403 (2007).

[5] F. Schmitt, P. S. Kirchmann, U. Bovensiepen, R. G. Moore, L. Rettig, M. Krenz, J. H. Chu, N. Ru, L. Perfetti, D. H. Lu, M. Wolf, I. R. Fisher, and Z. X. Shen, Transient electronic structure and melting of a charge density wave in $TbTe_3$, Science **321**, 1649 (2008).

[6] A. Soumyanarayanan, M. M. Yee, Y. He, J. van Wezel, D. J. Rahn, K. Rossnagel, E. W. Hudson, M. R. Norman, and J. E. Hoffman, Quantum phase transition from triangular to stripe charge order in $NbSe_2$, Proc. Natl. Acad. Sci. U. S. A. **110**, 1623 (2013).

[7] M. Lavagnini, H. M. Eiter, L. Tassini, B. Muschler, R. Hackl, R. Monnier, J. H. Chu, I. R. Fisher, and L. Degiorgi, Raman scattering evidence for a cascade evolution of the charge-density-wave collective amplitude mode, Phys. Rev. B **81**, 081101 (2010).

[8] P. Monceau, Electronic crystals: An experimental overview, Adv. Phys. **61**, 325 (2012).

[9] G. Grüner, The dynamics of charge-density waves, Rev. Mod. Phys. **60**, 1129 (1988).

[10] X. L. Wu and C. M. Lieber, Direct characterization of charge-density-wave defects in titanium-doped $TaSe_2$ by scanning tunneling microscopy, Phys. Rev. B **41**, 1239 (1990).

[11] H. J. Dai and C. M. Lieber, Charge density wave pinning and disorder in two dimensions, J. Phys. Chem. **97**, 2362 (1993).

[12] J.-i. Okamoto, C. J. Arguello, E. P. Rosenthal, A. N. Pasupathy, and A. J. Millis, Experimental Evidence for a Bragg Glass Density Wave Phase in a Transition-Metal Dichalcogenide, Phys. Rev. Lett. **114**, 026802 (2015).

[13] A. M. Novello, M. Spera, A. Scarfato, A. Ubaldini, E. Giannini, D. R. Bowler, and C. Renner, Stripe and Short Range Order in the Charge Density Wave of 1*T*-Cu_xTiSe_2, Phys. Rev. Lett. **118**, 017002 (2017).

[14] Y. I. Joe, X. M. Chen, P. Ghaemi, K. D. Finkelstein, G. A. de la Peña, Y. Gan, J. C. T. Lee, S. Yuan, J. Geck, G. J. MacDougall, T. C. Chiang, S. L. Cooper, E. Fradkin, and P. Abbamonte, Emergence of charge density wave domain walls above the superconducting dome in 1*T*-$TiSe_2$, Nat. Phys. **10**, 421 (2014).

[15] L. J. Li, E. C. O'Farrell, K. P. Loh, G. Eda, B. Ozyilmaz, and A. H. Castro Neto, Controlling many-body states by the electric-field effect in a two-dimensional material, Nature (London) **529**, 185 (2016).

[16] B. Hildebrand, T. Jaouen, C. Didiot, E. Razzoli, G. Monney, M. L. Mottas, A. Ubaldini, H. Berger, C. Barreteau, H. Beck, D. R. Bowler, and P. Aebi, Short-range phase coherence and origin of the 1*T*-$TiSe_2$ charge density wave, Phys. Rev. B **93**, 125140 (2016).

[17] H. J. Dai, H. F. Chen, and C. M. Lieber, Weak Pinning and Hexatic Order in a Doped Two-dimensional Charge-Density-Wave System, Phys. Rev. Lett. **66**, 3183 (1991).

[18] D. M. Oh and H. W. Yeom, Atomistic view of impurities interacting with a quasi-one-dimensional charge density wave, Phys. Rev. B **93**, 235448 (2016).

[19] H. W. Yeom, S. Takeda, E. Rotenberg, I. Matsuda, K. Horikoshi, J. Schaefer, C. M. Lee, S. D. Kevan, T. Ohta, T. Nagao, and S. Hasegawa, Instability and Charge Density Wave of Metallic Quantum Chains on a Silicon Surface, Phys. Rev. Lett. **82**, 4898 (1999).

[20] S. S. Lee, J. R. Ahn, N. D. Kim, J. H. Min, C. G. Hwang, J. W. Chung, H. W. Yeom, S. V. Ryjkov, and S. Hasegawa, Adsorbate-Induced Pinning of a Charge-Density Wave in a Quasi-1D Metallic Chains: Na on the In/Si(111)-(4 × 1) Surface, Phys. Rev. Lett. **88**, 196401 (2002).

[21] H. J. Dai and C. M. Lieber, Solid-Hexatic-Liquid Phases in Two-Dimensional Charge-Density Waves, Phys. Rev. Lett. **69**, 1576 (1992).

[22] T. H. Kim and H. W. Yeom, Topological Solitons Versus Nonsolitonic Phase Defects in a Quasi-One-Dimensional Charge-Density Wave, Phys. Rev. Lett. **109**, 246802 (2012).

[23] H. Morikawa, I. Matsuda, and S. Hasegawa, Direct observation of soliton dynamics in charge-density waves on a quasi-one-dimensional metallic surface, Phys. Rev. B **70**, 085412 (2004).

[24] M. H. Whangbo and E. Canadell, Analogies between the concepts of molecular chemistry and solid-state physics concerning structural instabilities. Electronic origin of the structural modulations in layered transition metal dichalcogenides, J. Am. Chem. Soc. **114**, 9587 (1992).

[25] X.-L. Wu, P. Zhou, and C. M. Lieber, Determination of the Local Effect of Impurities on the Charge-Density-Wave Phase in TaS_2 by Scanning Tunneling Microscopy, Phys. Rev. Lett. **61**, 2604 (1988).

[26] R. M. Fleming, D. E. Moncton, D. B. McWhan, and F. J. DiSalvo, Broken Hexagonal Symmetry in the Incommensurate Charge-Density Wave Structure of 2*H*-$TaSe_2$, Phys. Rev. Lett. **45**, 576 (1980).

[27] D. E. Moncton, J. D. Axe, and F. J. DiSalvo, Neutron scattering study of the charge-density wave transitions in 2*H*-$TaSe_2$ and 2*H*-$NbSe_2$, Phys. Rev. B **16**, 801 (1977).

[28] K.-i. Yokota, G. Kurata, T. Matsui, and H. Fukuyama, Superconductivity in the quasi-two-dimensional conductor 2*H*-$TaSe_2$, Physica B **284–288**, 551 (2000).

[29] L. J. Li, Y. P. Sun, X. D. Zhu, B. S. Wang, X. B. Zhu, Z. R. Yang, and W. H. Song, Growth and superconductivity of 2*H*-$Ni_{0.02}TaSe_2$ single crystals, Solid State Commun. **150**, 2248 (2010).

[30] D. Bhoi, S. Khim, W. Nam, B. S. Lee, C. Kim, B. G. Jeon, B. H. Min, S. Park, and K. H. Kim, Interplay of charge density wave and multiband superconductivity in 2*H*-Pd_xTaSe_2, Sci. Rep. **6**, 24068 (2016).

[31] G. Bian, T.-R. Chang, R. Sankar, S.-Y. Xu, H. Zheng, T. Neupert, C.-K. Chiu, S.-M. Huang, G. Chang, I. Belopolski, D. S. Sanchez, M. Neupane, N. Alidoust, C. Liu, B. Wang, C.-C. Lee, H.-T. Jeng, C. Zhang, Z. Yuan, S. Jia, A. Bansil, F. Chou, H. Lin, and M. Z. Hasan, Topological nodal-line fermions in spin-orbit metal $PbTaSe_2$, Nat. Commun. **7**, 10556 (2016).

[32] G. Bian, T.-R. Chang, H. Zheng, S. Velury, S.-Y. Xu, T. Neupert, C.-K. Chiu, S.-M. Huang, D. S. Sanchez, I. Belopolski, N. Alidoust, P.-J. Chen, G. Chang, A. Bansil, H.-T. Jeng, H. Lin, and M. Z. Hasan, Drumhead surface states and topological nodal-line fermions in $TlTaSe_2$, Phys. Rev. B **93**, 121113 (2016).

[33] Y. P. Li, Y. Wu, C. C. Xu, N. N. Liu, J. Ma, B. J. Lv, G. Yao, Y. Liu, H. Bai, X. H. Yang, L. Qiao, M. C. Li, L. J. Li, H. Xing, Y. B. Huang, J. Z. Ma, M. Shi, C. Cao, Y. Liu, C. H. Liu, J. F. Jia, and Z. A. Xu, Anisotropic gapping of topological Weyl rings in the charge-density-wave superconductor In_xTaSe_2, Sci. Bull. **66**, 243 (2021).

[34] G. Yao, M. C. Duan, N. N. Liu, Y. F. Wu, D. D. Guan, S. Y. Wang, H. Zheng, Y. Y. Li, C. H. Liu, and J. F. Jia, Diamagnetic Response of Potassium-Adsorbed Multilayer FeSe Film, Phys. Rev. Lett. **123**, 257001 (2019).

[35] Y. F. Wu, M. C. Duan, N. N. Liu, G. Yao, D. D. Guan, S. Y. Wang, Y. Y. Li, H. Zheng, C. H. Liu, and J. F. Jia, Diamagnetic response of a superconducting surface superstructure: Si(111)-$\sqrt{7}\times\sqrt{3}$-In, Phys. Rev. B **99**, 140506 (2019).

[36] G. Kresse and J. Hafner, Ab initio molecular dynamics for open-shell transition metals, Phys. Rev. B **48**, 13115 (1993).

[37] Z. Dai, Q. Xue, Y. Gong, C. G. Slough, and R. V. Coleman, Scanning-probe-microscopy studies of superlattice structures and density-wave structures in 2H-$NbSe_2$, 2H-$TaSe_2$, and 2H-TaS_2 induced by Fe doping, Phys. Rev. B **48**, 14543 (1993).

[38] S. C. Yan, D. Iaia, E. Morosan, E. Fradkin, P. Abbamonte, and V. Madhavan, Influence of Domain Walls in the Incommensurate Charge Density Wave State of Cu Intercalated 1*T*-$TiSe_2$, Phys. Rev. Lett. **118**, 106405 (2017).

[39] See Supplemental Material at http://link.aps.org/supplemental/10.1103/PhysRevB.104.235410 for detailed FFT analysis on subregions of the STM images.

[40] U. Chatterjee, J. Zhao, M. Iavarone, R. Di Capua, J. P. Castellan, G. Karapetrov, C. D. Malliakas, M. G. Kanatzidis, H. Claus, J. P. C. Ruff, F. Weber, J. van Wezel, J. C. Campuzano, R. Osborn, M. Randeria, N. Trivedi, M. R. Norman, and S. Rosenkranz, Emergence of coherence in the charge-density wave state of 2*H*-$NbSe_2$, Nat. Commun. **6**, 6313 (2015).

[41] W. L. McMillan, Theory of discommensurations and the commensurate-incommensurate charge-density-wave phase transition, Phys. Rev. B **14**, 1496 (1976).

[42] R. A. Molina and J. González, Surface and 3D Quantum Hall Effects from Engineering of Exceptional Points in Nodal-Line Semimetals, Phys. Rev. Lett. **120**, 146601 (2018).

[43] F. Tang, Y. Ren, P. Wang, R. Zhong, J. Schneeloch, S. A. Yang, K. Yang, P. A. Lee, G. Gu, Z. Qiao, and L. Zhang, Three-dimensional quantum Hall effect and metal–insulator transition in $ZrTe_5$, Nature (London) **569**, 537 (2019).

[44] Z. Wang and S.-C. Zhang, Chiral anomaly, charge density waves, and axion strings from Weyl semimetals, Phys. Rev. B **87**, 161107 (2013).

[45] J. Gooth, B. Bradlyn, S. Honnali, C. Schindler, N. Kumar, J. Noky, Y. Qi, C. Shekhar, Y. Sun, Z. Wang, B. A. Bernevig, and C. Felser, Axionic charge-density wave in the Weyl semimetal $(TaSe_4)_2I$, Nature (London) **575**, 315 (2019).